INTERNATIONAL JOURNAL FOR NUMERICAL METHODS IN FLUIDS
Int. J. Numer. Meth. Fluids 2002; **39**:1013–1036 (DOI: 10.1002/fld.359)

Towards entropy detection of anomalous mass and momentum exchange in incompressible fluid flow

G. F. Naterer[1,*,†] and D. Rinn[2,‡]

[1]*Department of Mechanical and Industrial Engineering, University of Manitoba, 15 Gillson Street, Winnipeg, Manitoba, Canada R3T 2N2*
[2]*Department of Mechanical Engineering, Lakehead University, 955 Oliver Road, Thunder Bay, Ontario, Canada P7B 5E1*

SUMMARY

An entropy-based approach is presented for assessment of computational accuracy in incompressible flow problems. It is shown that computational entropy can serve as an effective parameter in detecting erroneous or anomalous predictions of mass and momentum transport in the flow field. In the present paper, the fluid flow equations and second law of thermodynamics are discretized by a Galerkin finite-element method with linear, isoparametric triangular elements. It is shown that a weighted entropy residual is closely related to truncation error; this relationship is examined in an application problem involving incompressible flow through a converging channel. In particular, regions exhibiting anomalous flow behaviour, such as under-predicted velocities, appear together with analogous trends in the weighted entropy residual. It is anticipated that entropy-based error detection can provide important steps towards improved accuracy in computational fluid flow. Copyright © 2002 John Wiley & Sons, Ltd.

1. INTRODUCTION

The application of computational fluid dynamics (CFD) to fluids engineering design has become widespread during the past few decades. From the design of power generation and transmission systems to de-icing of helicopters and airplanes, and many other applications, CFD provides a key tool for the achievement of many technological goals. Although detailed experimentation, such as wind tunnel testing, is an important part of the advancement of these technologies, it may be too expensive or time consuming in many cases. Furthermore, in the absence of conclusive grid refinement studies, or available experimental or analytical (benchmark) data, the design engineer is often left with a dilemma in assessing whether certain local CFD predictions, such as a sudden flow reversal, are reasonable or perhaps non-physical, due to discretization or other modelling errors [1].

* Correspondence to: G. F. Naterer, Department of Mechanical and Industrial Engineering, University of Manitoba, 15 Gillson Street, Winnipeg, Manitoba, Canada R3T 2N2.
† Associate Professor.
‡ Research Assistant.

Contract/grant sponsor: Natural Sciences and Engineering Research Council of Canada

Received 8 December 2000
Revised 6 March 2002

Unlike the Euler and Navier–Stokes equations, relatively little attention has been devoted to the numerical discretization and potential importance of the second law in computational fluid flow. It is suspected that entropy computations are often neglected when design criteria are not directly linked to the second law. However, previous studies by Lax [2], Hughes and co-workers [3] and Camberos [4] have shown their importance. For example, the second law may provide a corrective measure for computations exhibiting non-physical predictions such as numerical oscillations (i.e. Naterer and Schneider [5]). Also, previous studies by Merriam [6] and Naterer and Camberos [7] have shown close relationships between the second law and overall accuracy and stability of fluid flow computations. In many situations, entropy can give deep insight into the overall behaviour of a particular engineering system. In this article, an entropy-based formulation will be described in the context of a Galerkin weighted residual method [8].

When striving to improve the numerical accuracy, grid refinements and/or higher-order interpolation within an element may be adopted. Error indicators are widely used to improve solution accuracy. Local *a posteriori* error estimates in finite-element analysis involve the assessment of solution errors by analysing the results after the computed solution is obtained. These methods are described in different levels of detail in various sources, including finite-element books of Akin [9] and Becker *et al*. [10]. Also, a comprehensive overview of error indicators for elliptic problems is documented by Babuska *et al*. [11].

The magnitude and distribution of finite-element errors can be predicted by certain functionals of the residual, involving an ellipticity condition of the governing differential operator [12]. A difficulty of evaluating certain norms in residual-based methods occurs when requiring local auxiliary problems to be formulated [13], thereby increasing the computational costs. Furthermore, the error estimates often involve optimal grids based on local gradients of the scalar variable [14], which can entail substantially more computational effort. An alternative to residual-based techniques uses interpolation error estimates, whereby higher-order derivatives of the unknown solution are computed throughout the mesh [15]. For example, second-order derivatives of the scalar variable are used for triangular elements in heat transfer and field problems [16]. Some applications to solid and fluid mechanics problems are presented by Oden *et al*. [17]. However, due to its complex post-processing, these methods are generally available for a limited class of field problems.

Thus, despite their advances, these error indicators have various limitations. They often require higher-order derivatives, which may be difficult or impractical to evaluate. In many cases, these derivatives may not be bounded. Also, a systematic way of calculating various constants in the error bounds of conventional error indicators is generally not known for a wide class of problems. As a result, an alternative entropy-based approach is considered in this article. In addition to potentially overcoming the aforementioned difficulties, its basis in the second law of thermodynamics may encompass all numerical errors, not just selected errors such as dispersive or false diffusion errors [18]. Other error indicators may be restricted to *h methods* or *p methods* [11], whereas the second law is applicable under both circumstances. Furthermore, unlike other methods, it may be used at both global and local levels of finite-element analysis.

Previous studies have shown that entropy can provide an effective tool for improved accuracy, including predictions involving viscous, compressible flows (i.e. Reference [19]) and fluid flow with phase change (i.e. Reference [20]). The goal of this article is to examine a more direct relationship between computational entropy and numerical error in a Galerkin

finite-element method. For inviscid and isothermal flow, it is expected that computational errors alone are responsible for production/destruction of entropy. In this article, an entropy formulation will be developed and applied to an incompressible flow problem to demonstrate its promising potential in assessing numerical errors.

2. PROBLEM FORMULATION

2.1. Governing equations

The Euler equations of fluid motion for incompressible, inviscid flow can be written as

$$\frac{\partial \mathbf{q}}{\partial t} + \frac{\partial \mathbf{f}}{\partial \mathbf{x}} = 0 \tag{1}$$

where the conserved variables, $\mathbf{q}$, and flux quantities, $\mathbf{f}$, are given by

$$\mathbf{q} = \begin{pmatrix} \rho \\ \rho u \\ \rho v \end{pmatrix}; \quad \mathbf{f} = \begin{bmatrix} \rho u & \rho v \\ \rho uu + p & \rho uv \\ \rho vu & \rho vv + p \end{bmatrix} \tag{2}$$

The bold font notation involving differentiation of the independent spatial variable, i.e. $\partial/\partial\mathbf{x}$, refers to the divergence operator in multi-dimensional problems (note: regular derivative in 1-D problems).

For steady inviscid flows, the governing equation becomes Laplace's equation, i.e.

$$\frac{\partial^2 \phi}{\partial x^2} + \frac{\partial^2 \phi}{\partial y^2} = 0 \tag{3}$$

where ϕ refers to the velocity potential. After ϕ is obtained from the solution of Equation (3), subject to appropriate boundary conditions, the velocity components can be computed by

$$u = \frac{\partial \phi}{\partial x}, \quad v = \frac{\partial \phi}{\partial y} \tag{4}$$

Alternatively, the governing equation may be written as Laplace's equation in terms of a stream function, ψ. Using a viscous–inviscid interaction (i.e. see Reference [1]), the potential flow solution may then be combined with an appropriate boundary layer solution to provide the complete behaviour of the external flow. In this article, only the inviscid flow will be examined in detail.

After adopting the velocity potential in the continuity equation, the momentum equations (i.e. Euler equations) become Bernoulli's equation, i.e.

$$p = p_0 + \frac{1}{2}\rho(V_0^2 - V^2) \tag{5}$$

where V represents total velocity magnitude and p_0 and V_0 refer to reference pressure and velocity values, respectively. We will use this Bernoulli equation to calculate pressure, based on the velocity results obtained from the solution of Laplace's equation.

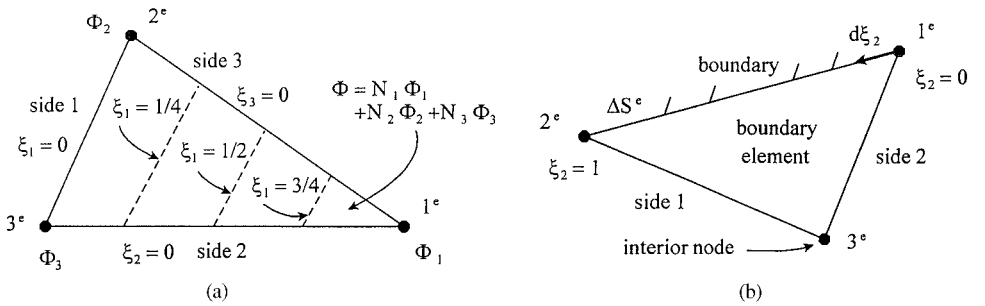

Figure 1. Schematic of sample (a) interior and (b) boundary element.

2.2. *Weighted residual method*

In the present work, Equation (3) will be solved with a weighted residual method involving a finite-element discretization. In this method, a trial function, such as a piecewise linear interpolation function, is selected to approximate the problem variable (ϕ). We will use the notations ϕ and $\tilde{\phi}$ to indicate exact and approximate (trial) functions, respectively. In substituting ϕ into Equation (3), we find that the right side of the equation is indeed zero since ϕ is the exact solution. However, substituting $\tilde{\phi}$ will generally yield a non-zero value on the right side of Equation (3) since $\tilde{\phi}$ is an approximate solution. The difference between these right-side values is an indication of solution error (called solution residual). A convenient way to assess this residual is by defining an operator, $\mathscr{L}$, acting on a scalar variable, such as ϕ or $\tilde{\phi}$, i.e.

$$\mathscr{L}(\phi) = \frac{\partial^2 \phi}{\partial x^2} + \frac{\partial^2 \phi}{\partial y^2} \tag{6}$$

In this way, the residual becomes $\mathscr{L}(\tilde{\phi})$.

In the weighted residual method, the residual is minimized over the domain after setting the integrated and weighted value of the residual to zero, i.e.

$$\int_{\mathscr{V}} W_i \mathscr{L}(\tilde{\phi})\, \mathrm{d}\mathscr{V} = \int_{\mathscr{V}} W_i R\, \mathrm{d}\mathscr{V} = 0 \tag{7}$$

where W_i, R and $\mathscr{V}$ refer to weight function, solution residual and volume of element (or area in two dimensions), respectively. In this paper, Galerkin's method is used to select the weight functions, whereby the weight functions equal the interpolation functions of the approximate solution.

2.3. *Finite element procedure*

Linear, isoparametric, triangular elements will be used in the two-dimensional discretization of the problem domain. Local co-ordinates (ξ_1, ξ_2, ξ_3) are defined within each element (see Figures 1(a) and (b)) and interpolation of scalar values within an element is based on the local shape functions, i.e.

$$\phi(x, y) = N_1 \Phi_1 + N_2 \Phi_2 + N_3 \Phi_3 \tag{8}$$

where uppercase Φ and N_i, $i=1,2,3$, refer to nodal value and shape function evaluated at position x, y (or ξ_1, ξ_2, ξ_3 in terms of local co-ordinates) within the element, respectively.

The shape functions are written in terms of the global co-ordinates, x and y, by

$$N_i = \frac{1}{2a}(a_i + b_i x + c_i y) \tag{9}$$

where

$$a_1 = x_2 y_3 - x_3 y_2, \quad b_1 = y_2 - y_3, \quad c_1 = x_3 - x_2 \tag{10}$$

$$a_2 = x_3 y_1 - x_1 y_3, \quad b_2 = y_3 - y_1, \quad c_2 = x_1 - x_3 \tag{11}$$

$$a_3 = x_1 y_2 - x_2 y_1, \quad b_2 = y_1 - y_2, \quad c_3 = x_2 - x_1 \tag{12}$$

and the subscripts for x and y refer to the local node within the element. Also, a denotes the area of the triangular element (note: $2a = a_1 + a_2 + a_3$). Furthermore, the derivatives of the linear shape functions are obtained from Equation (9), i.e.

$$\frac{\partial N_i}{\partial x} = \frac{b_i}{2a}, \quad \frac{\partial N_i}{\partial y} = \frac{c_i}{2a} \tag{13}$$

These results will now be applied to the discretization of the governing equation, Equation (6).

Applying Galerkin's weighted residual method, Equation (7), to the governing equation, Equation (6),

$$\int_{A^e} N_i \left[\frac{\partial}{\partial x} \left(\frac{\partial \tilde{\phi}}{\partial x} \right) \right] \mathrm{d}x^e \, \mathrm{d}y^e + \int_{A^e} N_i \left[\frac{\partial}{\partial y} \left(\frac{\partial \tilde{\phi}}{\partial y} \right) \right] \mathrm{d}x^e \, \mathrm{d}y^e = WR_i^e \tag{14}$$

where A and the superscript e refer to area and elemental value (i.e. local within element), respectively. Applying integration by parts to Equation (14), we obtain

$$\int_{S^e} \left[N_i \frac{\partial \tilde{\phi}}{\partial n} \right] \mathrm{d}S^e - \int_{A^e} \left[\frac{\partial N_i}{\partial x} \frac{\partial \tilde{\phi}}{\partial x} + \frac{\partial N_i}{\partial y} \frac{\partial \tilde{\phi}}{\partial y} \right] \mathrm{d}x^e \, \mathrm{d}y^e = WR_i^e \tag{15}$$

where the first and second integrals are line and area integrals, respectively.

Various boundary conditions can be represented in Equation (15) by specification of $\partial\tilde{\phi}/\partial n$ (derivative of $\tilde{\phi}$ in a direction normal to the boundary) along the boundary edge, S^e, in the first term. A sample boundary element on sides 1–2 is shown in Figure 1(b). In the evaluation of the line integral in Equation (15), the normal derivative is represented by

$$\frac{\partial \tilde{\phi}}{\partial n} = -B^e \tilde{\phi} + C^e \tag{16}$$

For example, a constant value of the derivative of $\tilde{\phi}$ (i.e $B^e = 0$ with non-zero C^e) is used to specify a fixed inlet velocity into the domain. The remaining assembly of elements and boundary conditions are completed based on conventional finite-element procedures [8]. In the following section, the finite-element procedure will be applied to the second law of thermodynamics, focusing mainly on its relevance in detecting anomalous trends in the numerical results.

3. SECOND LAW FORMULATION

Unlike the equality in the conservation equations, i.e. Equation (1), the second law involves an inequality (associated with production of entropy for irreversible processes) or equality (irreversible processes). In particular, the second law may be written in a similar form as Equation (1),

$$\frac{\partial S}{\partial t} + \frac{\partial \mathbf{F}}{\partial \mathbf{x}} = \dot{P}_s \tag{17}$$

where $S(\mathbf{q})$ and $\mathbf{F}(\mathbf{q})$ refer to entropy and entropy flux, respectively. For the Euler equations, these variables are given by $S = \rho s$ and $\mathbf{F} = \rho \mathbf{v} s$, respectively, where s refers to specific entropy. For irreversible processes, including isothermal, inviscid flow, the second law requires that the entropy production should equal zero. Otherwise, for irreversible processes such as viscous mixing in boundary layers or heat transfer, $\dot{P}_s$, is positive in Equation (17).

In addition to the second law, the entropy and entropy flux functions must satisfy two other important properties [2]. The first condition, involving downward concavity, is given by

$$S''(\mathbf{q}) < 0 \tag{18}$$

The second derivative of $S(\mathbf{q})$ is a negative definite matrix since irreversible processes produce entropy. In particular, entropy is bounded from above as it attains a maximum value at an equilibrium condition. Furthermore, the following second condition involves compatibility of the conserved and entropy flux variables, i.e.

$$\mathbf{F}'(\mathbf{q}) = S'(\mathbf{q})\mathbf{f}'(\mathbf{q}) \tag{19}$$

where $\mathbf{f}'(\mathbf{q})$ refers to the flux Jacobian (tensor of order 3) and $\mathbf{F}'(\mathbf{q})$ is the entropy flux derivative matrix. The compatibility condition in Equation (19) is an alternative way of expressing conservation of entropy for reversible processes.

In order to evaluate entropy in Equation (17), an entropy equation of state, involving pressure, is required. In this article, the entropy is written in terms of pressure, p, fluid density, ρ, and specific heat, c_v, in the following manner:

$$S = \rho s = \rho c_v \ln\left[\frac{p/p_0}{(\rho/\rho_0)^{c_p/c_v}}\right] \approx \rho c_v \ln\left[\frac{p}{p_0}\right] \tag{20}$$

where the subscript 0 refers to reference state. Equations (5) and (20) can be combined to give an expression involving entropy, pressure and velocity.

Then, the velocity components can be written in terms of the gradient of the velocity potential, thereby yielding the following result for entropy production from Equations (4), (5), (17) and (20),

$$\begin{aligned}\dot{P}_s = {} & \rho \frac{\partial \phi}{\partial x}\frac{\partial}{\partial x}\left[c_v \ln\left(1 + \frac{\rho}{2p_0}V_0^2 - \frac{\rho}{2p_0}\left(\frac{\partial \phi}{\partial x}\right)^2 - \frac{\rho}{2p_0}\left(\frac{\partial \phi}{\partial y}\right)^2\right)\right] \\ & + \rho \frac{\partial \phi}{\partial y}\frac{\partial}{\partial y}\left[c_v \ln\left(1 + \frac{\rho}{2p_0}V_0^2 - \frac{\rho}{2p_0}\left(\frac{\partial \phi}{\partial x}\right)^2 - \frac{\rho}{2p_0}\left(\frac{\partial \phi}{\partial y}\right)^2\right)\right]\end{aligned} \tag{21}$$

Performing the differentiation in both terms, we obtain

$$\dot{P}_s \approx -\frac{c_v \rho^2}{p}\left[u^2\left(\frac{\partial^2\phi}{\partial x^2}\right) + V_0(u+v)\left(\frac{\partial^2\phi}{\partial x \partial y}\right) + v^2\left(\frac{\partial^2\phi}{\partial y^2}\right)\right] \tag{22}$$

where V_0 refers to reference velocity, such as a specified inlet velocity.

After ϕ and its derivatives are obtained from the solution of Equation (3), the velocity components can be calculated based on Equation (4) and so the entropy production can be computed from Equation (22). Although the analytic solution would give a zero entropy production for incompressible, inviscid flow, the numerical solution may give a non-zero value since truncation errors may artificially produce (or destroy) entropy in the flow field. It is anticipated that this 'artificial' entropy production (or destruction) is closely related to non-physical or anomalous trends in predicted momentum exchange, such as velocity undershoots, in the flow field. It will be shown that entropy computations can be monitored to detect local anomalies and numerical errors in the flow field predictions. The magnitude of computational entropy production (or destruction) can provide a quantitative measure of these discrepancies through truncation errors in the local flow computations.

The computation of entropy will be based on our earlier Galerkin's method. Recall that the method of weighted residuals seeks to find the unknown coefficients in the trial function, $\tilde{\phi}$, by forming a weighted average of the solution error and specifying that this weighted average vanish in some average sense across the entire problem domain. It is anticipated that the corresponding weighted residual form of the entropy equation would not violate the second law if the interpolation and weight functions provided the exact distribution of ϕ within the domain. For example, linear velocity interpolation functions should yield exact results in the case of Couette channel flow [21] where a linear velocity profile is observed under appropriate boundary conditions. However, if the same interpolation functions are adopted in viscous flow through a pipe, then discrete errors in the weighted residual would arise since piecewise linear profiles are selected to approximate an essentially parabolic velocity distribution (laminar, fully developed flow [21]). This discrepancy between actual and computed profiles would not be detected in the weighted residual formulation of the conservation equations because the minimization of the resulting residual is used to compute the unknown coefficients forming the solution itself.

As a result, it is anticipated that an additional entropy principle can utilize the selected weight and interpolation functions to assess numerical accuracy by testing their relative magnitude by an equivalent weighted residual discretization of the second law. In a similar way as the derivation of Equation (14), we obtain the following weighted residual equation based on Equation (22),

$$-\int_A N_i K\left[u^2\left(\frac{\partial^2\tilde{\phi}}{\partial x^2}\right) + V_0(u+v)\left(\frac{\partial^2\tilde{\phi}}{\partial x \partial y}\right) + v^2\left(\frac{\partial^2\tilde{\phi}}{\partial y^2}\right)\right] \mathrm{d}A = \int_A W_i R \,\mathrm{d}A \tag{23}$$

where $K = -c_v\rho^2/p$. For brevity, the overbar tilde notation in the description of the approximate function, $\tilde{\phi}$, will be dropped in subsequent equations (replaced by ϕ).

Expanding the left side of Equation (23),

$$Ku^2 \int_A \frac{\partial}{\partial x}\left(N_i \frac{\partial \phi}{\partial x}\right) \mathrm{d}A - Ku^2 \int_A \frac{\partial N_i}{\partial x}\left(\frac{\partial \phi}{\partial x}\right) \mathrm{d}A + KV_0(u+v) \int_A \frac{\partial}{\partial x}\left(N_i \frac{\partial \phi}{\partial y}\right) \mathrm{d}A$$
$$-KV_0(u+v) \int_A \frac{\partial N_i}{\partial x}\left(\frac{\partial \phi}{\partial y}\right) \mathrm{d}A + Kv^2 \int_A \frac{\partial}{\partial y}\left(N_i \frac{\partial \phi}{\partial y}\right) \mathrm{d}A$$
$$-Kv^2 \int_A \frac{\partial N_i}{\partial y}\left(\frac{\partial \phi}{\partial y}\right) \mathrm{d}A = \mathrm{WER}_i \tag{24}$$

where WER_i refers to weighted entropy residual (node i), based on the right side of Equation (23). It should be noted that W and R in WER do not refer to weight function and residual, respectively, in the sense of individual expressions, but rather as words in the acronym. Applying integration by parts to the first, third and fifth terms in Equation (24), we obtain weighted entropy flux terms across the edges of an element. After assembly of all finite elements, these boundary terms are added in the global equations only in elements with sides along external domain boundaries. Since it is anticipated that computational errors arise largely due to numerical discretization within the domain, rather than specification of boundary conditions, we will focus our attention on the interior terms only.

For isoparametric, triangular elements, the spatial derivative terms in Equation (23) can be readily evaluated. The values of ϕ and its derivatives will be approximated in the following way:

$$\phi = \sum_{j=1}^{3} N_j \phi_j; \quad \frac{\partial \phi}{\partial x} = \sum_{j=1}^{3} \frac{\partial N_j}{\partial x} \phi_j \tag{25}$$

A similar expression is obtained for the y derivative. Substituting Equation (25) into Equation (24),

$$-K \int_A \sum_{j=1}^{3} \left[\frac{\partial N_i}{\partial x}\frac{\partial N_j}{\partial x}\phi_j u^2 + \frac{\partial N_i}{\partial x}\frac{\partial N_j}{\partial y}\phi_j V_0(u+v) + \frac{\partial N_i}{\partial y}\frac{\partial N_j}{\partial y}\phi_j v^2\right] \mathrm{d}A = \mathrm{WER}_i \tag{26}$$

In Equation (26), the subscripts i and j can be interpreted as row and column, respectively, within the local stiffness matrix for the entropy equation.

Recall that the partial derivatives of ϕ are given by constant values in Equation (13). Substituting these values into Equation (26), we obtain the following 3×3 local stiffness matrix, G_{ij}, and entropy stiffness equation

$$K[G^e]\{\Phi^e\} = \{\mathrm{WER}^e\} \tag{27}$$

where

$$G_{ij}^e = b_i b_j u^2 + b_j c_i V_0(u+v) + c_i c_j v^2 \tag{28}$$

In the same way as the assembly of elements for the conservation equations, the above local stiffness matrix is computed for each element and then assembled into the global stiffness matrix in accordance with the mapping between local and global nodes in the mesh.

In particular, the weighted entropy residual at node i is obtained by

$$\mathrm{WER}_i = \sum_{e=1}^{nel} \sum_{j=1}^{nnpe} G_{ij}^e \Phi_j^e \tag{29}$$

where contributions of various WER^e terms to a particular global node are obtained after assembly of all elements. In Equation (29), addition of a term on the right side to node i is only included if local node j in element e corresponds to global node i. Also, the summations are performed over *nel* (number of elements) and *nnpe* (number of nodal points per element).

Although the weighted residual term vanished after assembly of elements following Equation (15), an analogous zero summation does not directly apply to the assembly procedure involving Equation (27). Recall that the unknown nodal Φ values were obtained to provide a zero weighted residual in the conservation equation, Equation (7). On the other hand, these nodal Φ values are then substituted into the equivalent entropy form of Equation (7), where the discrete operator is instead based on Equations (21)–(22). In this case, the nodal Φ values are no longer unknown quantities (unlike solution of conservation equation). As a result, the nodal Φ values are effectively tested in this way to find the resulting WER proximity to zero (expected value for potential flow) following the assembly of all elements.

Equation (27) indicates that the weighted entropy residual is computed by multiplication of the stiffness matrix by the column vector of nodal potential function values. These calculations give a value of weighted entropy residual at the corresponding global node. In particular, the values of the global stiffness matrix and potential function distribution must be known prior to the entropy analysis. In this way, the entropy analysis is de-coupled from the initial finite-element solution involving ϕ. Although it is de-coupled, it will be shown that it can provide a useful error detection mechanism, and a possible corrective step in the computations to improve solution accuracy at subsequent iterations or time steps in transient problems.

4. ENTROPY-BASED ERROR ANALYSIS

In this section, we will develop a relationship between truncation error in the discrete solution and weighted entropy residual (as discussed in the previous section). Although the analysis here will only consider a one-dimensional form of the governing equations and domain, it is anticipated that the results can be readily extended to two-dimensional problems by including an additional y direction derivative in the analysis. Also, the general case of transient problems will be considered here. The transient result can be readily simplified to a steady-state situation (previous section) by dropping the time dependent terms.

Recall the following conservation form of the governing Euler equations

$$\mathscr{L}^a(\mathbf{q}) = \frac{\partial \mathbf{q}}{\partial t} + \frac{\partial \mathbf{f}}{\partial x} \tag{30}$$

where $\mathbf{q}$, $\mathbf{f}$, $\mathscr{L}$ and superscript a refer to state and flux variables, operator and analytic, respectively. In Equation (30), the analytical operator, $\mathscr{L}^a(\mathbf{q})$, acts on $\mathbf{q}$, and yields a zero residual since $\mathbf{q}$ represents the exact solution. However, in the finite-element formulation, the discrete operator $\mathscr{L}^d(\tilde{\mathbf{q}})$ (acting on the approximate solution $\tilde{\mathbf{q}}$) generally gives a non-zero residual since the approximate solution typically differs from the exact solution. This discrepancy

may arise from various factors, such as inadequate interpolation in the computations. Based on backward differencing in time, and linear interpolation, the following discrete operator is obtained, based on discretization of Equation (30),

$$\mathscr{L}^d(\mathbf{q}) = \frac{\mathbf{q}_i^n - \mathbf{q}_i^{n-1}}{\Delta t} + \frac{\mathbf{f}_i^n - \mathbf{f}_{i-1}^n}{\Delta x} \tag{31}$$

where the overbar tilde notation is dropped in the discrete analysis for brevity since it can be implicitly understood that the discrete operator acts on the approximate solution, $\tilde{\mathbf{q}}$.

Using Taylor series expansions,

$$\mathbf{q}_i^n = \mathbf{q}_i^{n-1} + \Delta t \left.\frac{\partial \mathbf{q}}{\partial t}\right|^{n-1} + \frac{\Delta t^2}{2} \left.\frac{\partial^2 \mathbf{q}}{\partial t^2}\right|^{n-1} + \cdots \tag{32}$$

$$\mathbf{f}_{i-1} = \mathbf{f}_i - \Delta x \left.\frac{\partial \mathbf{f}}{\partial x}\right|_i + \frac{\Delta x^2}{2} \left.\frac{\partial^2 \mathbf{f}}{\partial x^2}\right|_i - \cdots \tag{33}$$

Substituting these expansions into Equation (31), and comparing with the terms in the analytic operator Equation (30), we obtain

$$\mathscr{L}^d(\mathbf{q}) = \mathscr{L}^a(\mathbf{q}) - \frac{\Delta x^2}{2} \left.\frac{\partial^2 \mathbf{f}}{\partial x^2}\right|_i + \frac{\Delta t^2}{2} \left.\frac{\partial^2 \mathbf{q}}{\partial t^2}\right|^{n-1} + \cdots \tag{34}$$

Alternatively, Equation (34) can be written in the following compact form:

$$\mathscr{L}^d(\mathbf{q}) = \mathscr{L}^a(\mathbf{q}) - \text{HOT} \tag{35}$$

where HOT refers to higher-order terms resulting from the Taylor series expansion in Equations (32)–(33). In particular, Equations (34)–(35) indicate that the discrete operator depends on the second-order temporal and spatial derivatives of $\mathbf{q}$ and other higher-order terms.

It will now be shown that truncation errors associated with the higher-order terms in Equation (35) can be directly related to the weighted entropy residual obtained earlier in Equation (27). In particular, truncation errors often yield anomalies (i.e. velocity overshoots/undershoots) in the computational predictions. Since the second law is expected to be sensitive to this type of occurrence, it is anticipated that the weighted entropy residual can detect non-physical anomalies in the computed results. Previous researchers have provided some evidence of this hypothesis and the role of entropy in stable computations. For example, recent developments have demonstrated that satisfaction of the second law is closely linked to upwinding accuracy (i.e. Reference [19]). Furthermore, it has been shown that the second law can provide a quantitative measure for identifying anomalous velocity overshoots in gas dynamics (i.e. Reference [5]). The goal of this section is to seek a more direct connection between truncation error and weighted entropy residual. In this way, the significance and impact of entropy in computational fluid flow can be further strengthened.

Pre-multiplying the discretization operator by $\partial S/\partial \mathbf{q}$ in Equation (34) gives the following expression for the entropy-weighted discretization error:

$$\frac{\partial S}{\partial \mathbf{q}} \mathscr{L}^d(\mathbf{q}) = \frac{\partial S}{\partial \mathbf{q}} \frac{\partial \mathbf{q}}{\partial t} + \frac{\partial S}{\partial \mathbf{q}} \frac{\partial \mathbf{f}}{\partial x} - \frac{\partial S}{\partial \mathbf{q}} (\text{HOT}) \tag{36}$$

In this equation, the derivative of $\mathbf{f}$ on the right side can be expanded as $\mathbf{f}'(\mathbf{q})$ multiplied by $\partial\mathbf{q}/\partial x$ using the chain rule of calculus. Furthermore, using the compatibility condition in Equation (19), as well as the chain rule, we obtain

$$\frac{\partial S}{\partial \mathbf{q}} \mathscr{L}^d(\mathbf{q}) = \frac{\partial S}{\partial t} + \frac{\partial \mathbf{F}}{\partial \mathbf{q}} \frac{\partial \mathbf{q}}{\partial x} - \frac{\partial S}{\partial \mathbf{q}} (\mathrm{HOT}) \tag{37}$$

From Equations (17) and (37), it can be observed that the first two terms on the right side of Equation (37) can be written as the entropy production rate, $\dot{P}_s$.

The numerical solution of Equation (31) is obtained by setting $\mathscr{L}^d(\mathbf{q}) = 0$, so the left side of Equation (37) is approximated as zero. The remaining terms yield the following result:

$$\dot{P}_s = \frac{\partial S}{\partial \mathbf{q}} (\mathrm{TE}) \tag{38}$$

where TE refers to truncation errors arising from neglected higher-order terms in the numerical formulation. The result in Equation (38) confirms an expected trend involving entropy and truncation error. For inviscid flows, it indicates that less computational entropy is produced when the grid spacing is reduced (i.e. truncation error decreases), while less entropy destruction would be anticipated for the analogous case with viscous flows. In this analysis, the magnitude of $\dot{P}_s$ refers to absolute difference between computed and expected entropy production (i.e. zero expected $\dot{P}_s$ for potential flow), whereas the magnitude and sign of $\dot{P}_s$ would be adopted for viscous flows. Furthermore, an important benefit of Equation (38) arises because it is de-coupled from the solution of the conservation equation, in the sense that ϕ is obtained independently of $\dot{P}_s$. As a result, $\dot{P}_s$ can be used as an independent detection of truncation errors, as well as a design variable for other applications, such as process optimization.

Comparing Equation (38) with the result leading to Equation (23), we then obtain the following relationship between truncation error and weighted entropy residual:

$$\int_A N_i \frac{\partial S}{\partial \mathbf{q}} (\mathrm{TE})\, \mathrm{d}A \approx \mathrm{WER}_i \tag{39}$$

where the left side of the equation represents a column vector (with entry i corresponding to node i) for a weighted truncation error (WTE). This result indicates that the weighted truncation error scales as the weighted entropy residual. It should be noted that entropy is implicitly coupled to other variables, including velocity and pressure through the Bernoulli equation and Equation (20), thereby providing a non-zero factor, $\partial S/\partial \mathbf{q}$, in Equation (39).

At this time, it is worthwhile to compare this entropy-based approach with other conventional methods of error analysis. For example, in Taylor series-based error analysis (alone; without analogy to entropy), the power (exponent) of the leading truncated term in the discrete formulation indicates the order of accuracy and truncation error in the model [1]. False diffusion errors arising when a flow is oblique to the grid lines can be assessed through a false diffusion coefficient, which describes the cross-stream diffusion arising from errors in the convection modelling [18]. These two methods apply to truncation and false diffusion errors, respectively; however, many other sources of error affect the results, i.e. discretization (interpolation for geometry and solution variables), spatial and temporal integration, iterations, round-off, etc.

Error analysis with one type of approach is often not feasible for other sources of error. In this way, the current entropy-based approach offers the following potential advantages over the previously described methods:

- Taylor series analysis is mathematically based, thereby often lacking physical interpretation; entropy and the second law can offer new physical insight into solution errors.
- The second law can provide a systematic, unified framework that can encompass both overall and individual approximation errors in the formulation [19].
- Taylor truncation errors are typically assessed after a solution is obtained, whereas entropy can be used as an active, rather than passive, variable in the error reduction [20].
- Taylor series methods alone (without analogy to entropy) are limited in view of terms discretized with different orders of accuracy. For example, convective terms may have a higher-order representation than diffusive terms. On the other hand, the magnitude of computed entropy production (or destruction) is a potentially effective alternative for measuring all types of errors since entropy is functionally dependent on all state variables.

Although the present paper only addresses truncation errors, it is anticipated that the entropy-based approach provides a solid foundation from which future advances (involving other types of solution errors) can be realized. In the following section, this entropy analysis will be applied to an example problem involving incompressible flow within a converging channel. It will be shown that numerical errors are closely related to the weighted entropy residual.

5. NUMERICAL RESULTS AND DISCUSSION

The problem considered in this section involves incompressible flow through a converging channel (see Figure 2(a)). Based on the method of superposition of potential flow solutions and conformal mapping, an analytical solution is obtained by combining the velocity potential functions, or equivalently, stream functions, ψ, for uniform and doublet flows. This superposition is similar to the construction of a Rankine oval [21], based on combined uniform and line source potential flows. In this case, symmetric doublets are added to simulate the upper parallel boundary in the current case. In an actual channel flow, a no-slip boundary condition is required at the top boundary (fixed wall), but in the present inviscid flow simulation, only a zero lateral (v component) velocity is set as zero. In practise, a viscous–inviscid interaction would be required (as discussed earlier), but the main focus of the current example will be the inviscid core region.

After combining the functions in the fashion described above, we obtain

$$\psi = V_0 y - V_0 y \left[\frac{R^2}{x^2 + y^2}\right] - V_0(y - 2h)\left[\frac{R^2}{x^2 + (y - 2h)^2}\right] - V_0(y + 2h)\left[\frac{R^2}{x^2 + (y + 2h)^2}\right] \quad (40)$$

where R and h refer to cylinder radius (see quarter cylinder centred at origin in Figure 2(a)) and channel height, respectively. Differentiating the stream function in Equation (40), the

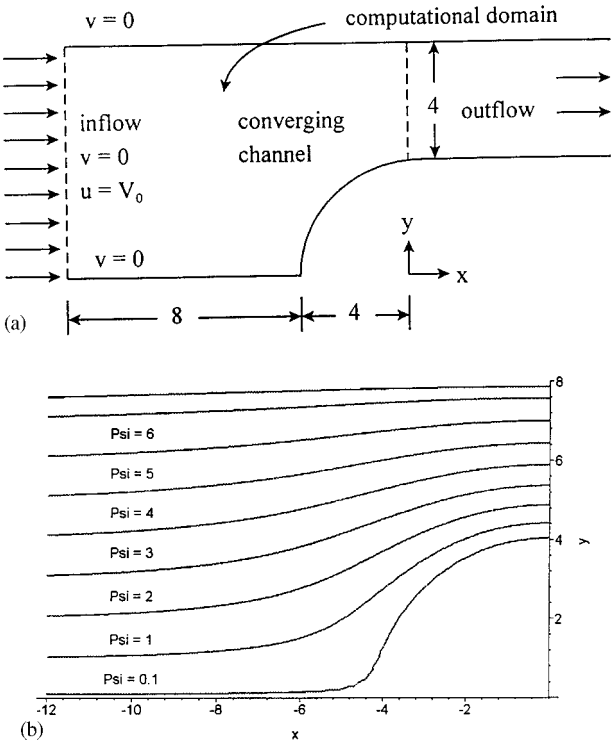

Figure 2. Schematic of (a) channel region and (b) analytical solution with streamlines.

following solutions are obtained for the local velocity components:

$$u = \frac{\partial \psi}{\partial y} = V_0 - \frac{V_0}{\lambda(x^2 + y^2)} + 2\frac{V_0 y^2}{\lambda(x^2 + y^2)^2} - \frac{V_0}{\lambda(x^2 + (y-2h)^2)} + \frac{V_0(y-2h)(2y-4h)}{\lambda(x^2 + (y-2h)^2)^2} - \frac{V_0}{\lambda(x^2 + (y+2h)^2)} + \frac{V_0(y+2h)(2y+4h)}{\lambda(x^2 + (y+2h)^2)^2} \tag{41}$$

$$v = -\frac{\partial \psi}{\partial x} = -2\frac{V_0 R y x}{\lambda(x^2 + y^2)^2} - 2\frac{V_0(y-2h)x}{\lambda(x^2 + (y-2h)^2)^2} - 2\frac{V_0(y+2h)x}{\lambda(x^2 + (y+2h)^2)^2} \tag{42}$$

where

$$\lambda = \frac{V_0 R}{1/R + 1/(R-2h) + 1/(R+2h)} \tag{43}$$

The computational domain is taken between $x = -12$ and $x = 0$ from $y = 0$ to $y = 8$ (see Figure 2(a)). The analytical solution (stream function contour lines) is illustrated in Figure 2(b). It will be observed that truncation errors, based on a comparison between computed results

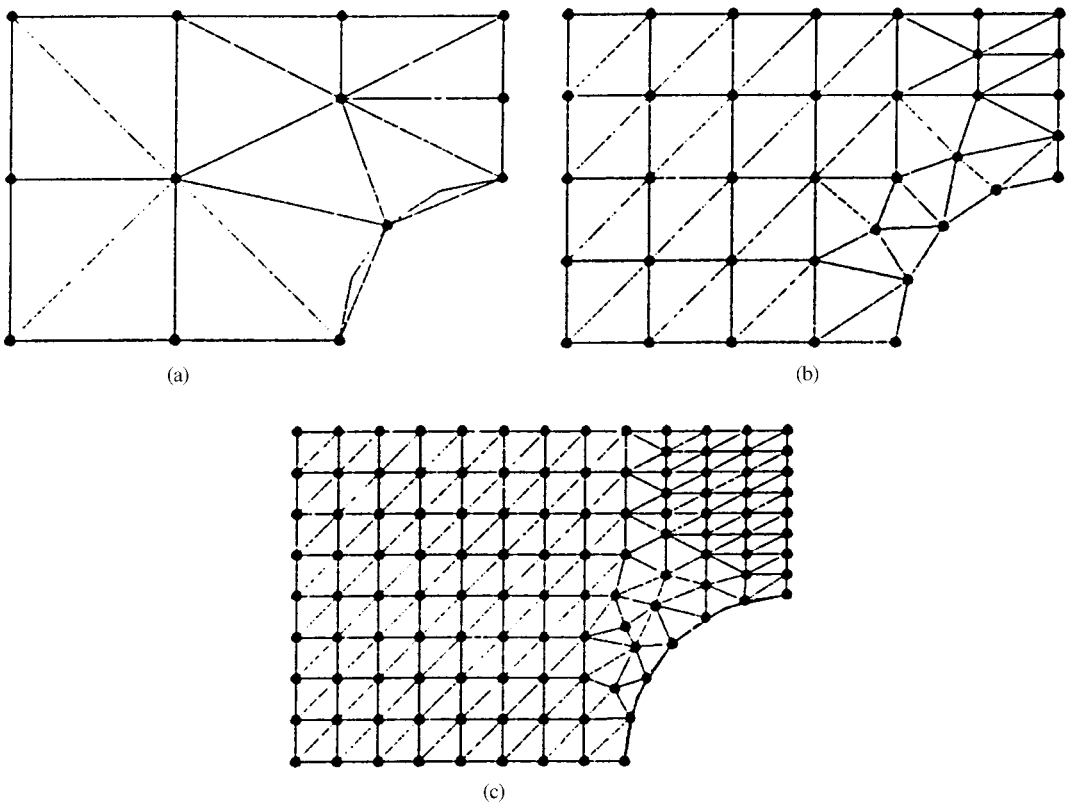

Figure 3. Configurations for (a) mesh 1, (b) mesh 2 and (c) mesh 3.

and the exact solution, and anomalies are closely linked with the weighted entropy residual and the second law.

Three mesh configurations will be examined in the current studies (see Figure 3). The grid spacing in the x and y directions is effectively reduced by a factor of 2 in each case and grids 1, 2 and 3 contain 13, 50 and 194 elements, respectively. The inlet pressure, p_0, and velocity, V_0, are specified as 100 kPa (atmospheric pressure, i.e. zero gage pressure) and 1 m/s, respectively. The density of air is taken as 1.2 kg/m^3 at standard atmospheric conditions.

Although zero entropy production is expected in this inviscid flow problem, it is the computed deviation from this expected value that can serve as a quantitative measure of anomalous solution behaviour. Since analytical (or known) entropy distributions are generally not available in many flow conditions, including viscous, turbulent flows, the deviations from expected behaviour can be quantified in the sense that the magnitude of computed negative entropy production would be an indication of anomalous results. These anomalous results may arise from discretization errors such as errors due to inadequate spatial or temporal differencing in the overall formulation.

The computed results involving total velocity magnitude, V, and normalized, weighted entropy residual will now be presented (Figures 4–5) along horizontal and vertical

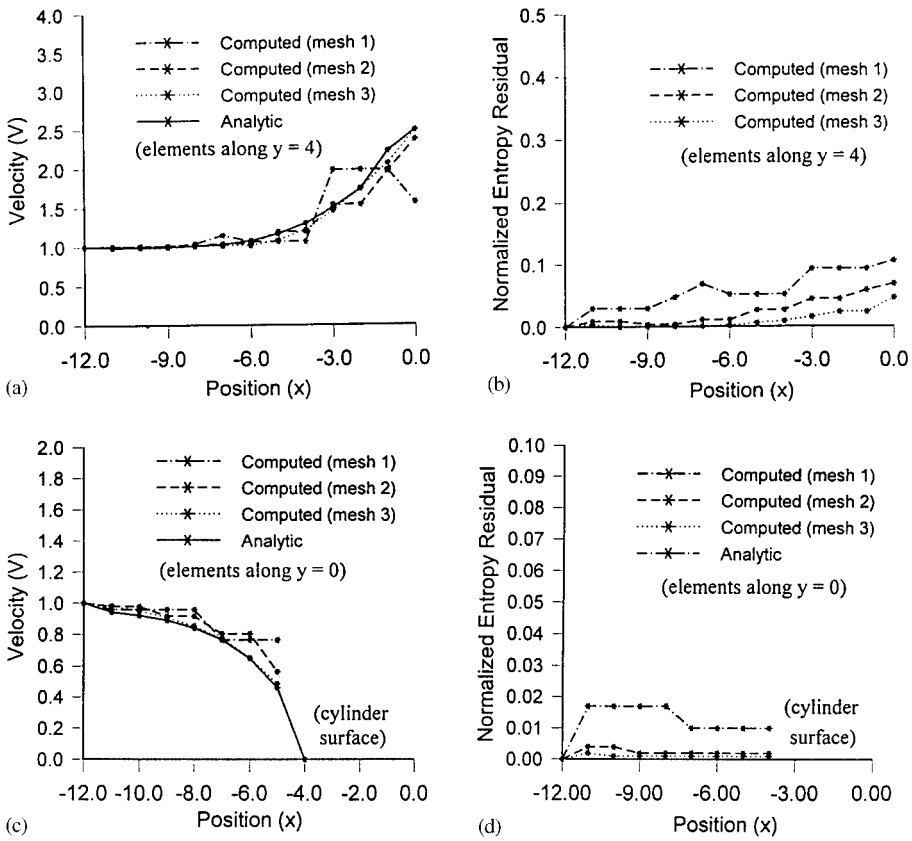

Figure 4. Velocity and normalized entropy residual results along (a)–(b) $y=4$ and (c)–(d) $y=0$.

sections of the domain. In particular, the results will be displayed for elements along two horizontal lines, i.e. $y=4$ and bottom boundary, $y=0$ (Figure 4), and two vertical lines, i.e. $x=-9$ and outflow boundary, $x=0$ (Figure 5). In these figures, it will be shown that the diminishing solution error with grid refinement is closely related to a diminishing WER magnitude.

Along $y=4$, the velocity magnitude increases when x increases since the fluid experiences an area contraction within the channel (see Figure 2(a)). In Figure 4(a), the computed results agree well with the analytical solution as grid refinement is effected. Although large solution errors are observed for the coarse grid (mesh 1), these computed errors are largely reduced in the finite-element results for the fine grid (mesh 3). Larger solution errors (coarse mesh) are observed in the contracting region above the cylinder. This result is not surprising in the sense that the flow character is changing more rapidly there (i.e. in comparison to inlet region near $x=-12$) and thus more grid refinement is required for adequate resolution in regions exhibiting rapid flow variations. In addition to reduced solution error after grid refinement in Figure 4(a), the proper trends in the data are observed, i.e. monotonically increasing velocity magnitude through the converging channel.

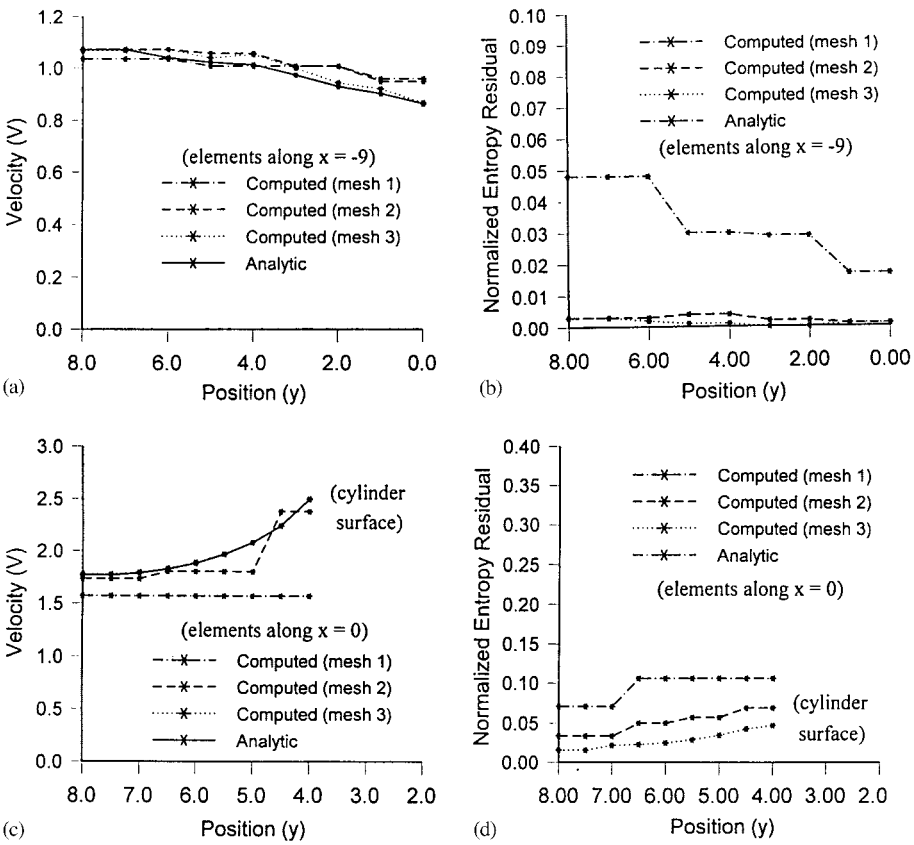

Figure 5. Velocity and normalized entropy residual results along (a)–(b) $x = -9$ and (c)–(d) $x = 0$.

In Figure 4(b), the entropy residual results (normalized with respect to a reference WER, i.e. total computed WER in the domain) are illustrated. It can be observed that the normalized WER is reduced as the grid is refined to a smaller mesh spacing. In other words, the reduction of solution error in Figure 4(a) closely coincides with the rate of WER reduction in the computed entropy results. The significance of this observation is that WER can provide a quantitative measure of truncation error in more practical circumstances where an analytical solution is not available for comparison purposes. For example, in the absence of experimental data or analytical benchmark results (commonly experienced in industrial fluid flow problems), the current results indicate that the computed WER can provide some evidence regarding the reliability, accuracy and physical plausibility of the numerical results.

The absolute value of WER is reported in the current results since either a positive or negative deviation from zero entropy production is considered erroneous for incompressible, potential flow. This approach can be readily modified to more complex flows, such as viscous, turbulent flows, by considering the erroneous deviation as computed negative entropy production since these computations would violate the second law. Furthermore, the magnitude and overall trends in computed WER results appear closely related to local flow anomalies. For

example, the decreased velocity at the outlet (mesh 1) in Figure 4(a) is clearly non-physical since the fluid experiences an area contraction. This local flow anomaly is detected by an increased WER to a maximum computed WER at the outlet section in Figure 4(b). It appears that local WER computations can detect anomalous trends in fluid flow predictions without knowledge (*a priori*) of the expected or exact results.

In a similar way, the results in Figures 4(c)–4(d) illustrate predicted velocity and WER results along the bottom boundary (elements along $y = 0$). In this case, the velocity decreases from its specified inlet value to zero at the stagnation point in front of the cylinder surface. Although the computed stagnation zero velocity satisfies the boundary condition (zero fluid penetration through wall), it lies within the boundary layer region, i.e. not inviscid region as examined and shown here. The results again illustrate the reduced solution error and computed WER magnitude as grid refinement is effected (i.e. smallest error with results from mesh 3). If an analytical solution was not available, then the WER results in Figure 4(b) would correctly detect anomalous results at $x = -5$ from mesh 1 and higher solution errors than predictions with mesh 3 at the same position since the WER is approximately an order of magnitude smaller in the latter case. Based on Figure 4(c), these detected anomalies would be correct since an erroneous constant velocity profile is predicted for mesh 1 (between $x = -7$ and -5) whereas mass and momentum exchange at this location requires a sharp decrease in velocity as the surface of the cylinder is approached.

It should be emphasized that the entropy-based approach provides a quantitative measure of this anomalous behaviour and thus it provides a potentially predictive mechanism for corrections and/or suitable adjustments of the computations. In addition to computational fluid flow, it is anticipated that this type of error detection and predictive entropy correction could be applied to a variety of other engineering applications, including thermal/fluid control systems or signal processing. As a result, although the current example is limited to incompressible, potential flow, it is anticipated that the entropy-based approach can be applied and extended to other practical problems.

In Figure 5, results along $x = -9$ are presented for velocity magnitude (Figure 5(a)) and normalized entropy residual (Figure 5(b)). In this case, the velocity magnitude is lower at $y = 0$ (bottom boundary) in comparison to $y = 8$ (top boundary) since the flow decelerates to a stagnation point in front of the cylinder along $y = 0$, whereas the flow is not obstructed in this manner along the top boundary. The solution error is reduced in grid 3 in Figure 5(a) (smallest grid spacing), and the smallest computed WER magnitude (Figure 5(b)) coincides with this observation. Similar trends are observed for results along the outlet boundary at $x = 0$ for velocity magnitude (Figure 5(c)) and normalized WER (Figure 5(d)). In this case, the effects of grid spacing are most clearly observed, where significant discrepancy with analytical results is obtained with the coarse grid (mesh 1), while good agreement between computed and analytical results is achieved with the refined grid (mesh 3).

The weighted entropy residual results at the outflow boundary are illustrated in Figure 5(d). It should be noted that our entropy analysis has predicted that truncation error was proportional to WER, but the constant of proportionality was dependent on the local entropy derivative (with respect to $\mathbf{q}$). The proportionality aspect is correctly predicted in the sense that reductions in solution error and WER appear closely related. Thus, anomalous results can be detected in the sense of WER comparisons between results from mesh 1 (higher WER) and mesh 3 (lower WER and lower solution error). Rather than expecting precise error values based on the WER results, these WER results are instead aimed to provide a tool for error analysis

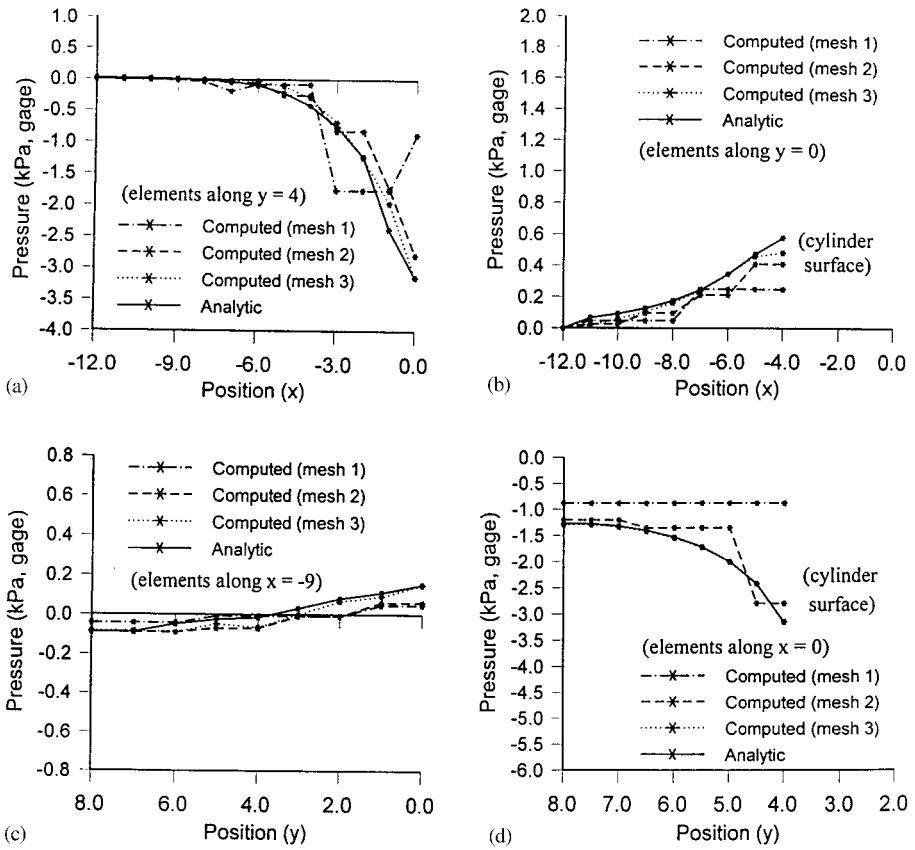

Figure 6. Pressure results along (a) $y=4$, (b) $y=0$, (c) $x=-9$, and (d) $x=0$.

and generally detecting overall trends involving non-physical or anomalous results in the flow computations.

Pressure results (in terms of gage pressure, kPa) are illustrated in Figure 6. In particular, pressure results along $y=4$, $y=0$, $x=-9$ and $x=0$ are illustrated in Figures 6(a)–6(d), respectively. From Bernoulli's equation, it can be observed that an increased velocity (relative to reference velocity, or incoming velocity, V_0) coincides with a pressure decrease (relative to reference pressure, i.e. atmospheric pressure). As a result, pressure decreases (Figure 6(a)) as velocity increases (Figure 4(a)) along $y=4$; analogous trends are observed in Figures 6(b)–6(d). In all cases, the predicted pressure results approach the analytical solution as the grid is refined.

Important trends in solution error and entropy residual at the outflow boundary ($x=0$) are summarized in Figures 7(a)–7(b), respectively (note: log–log axes). Close similarities are observed in the trends of both figures. In Figure 7(a), the solution error is based on the absolute difference between computed and exact (subscript ex) results of velocity magnitude at various y positions at the outflow boundary ($x=0$). The different y positions are indicated

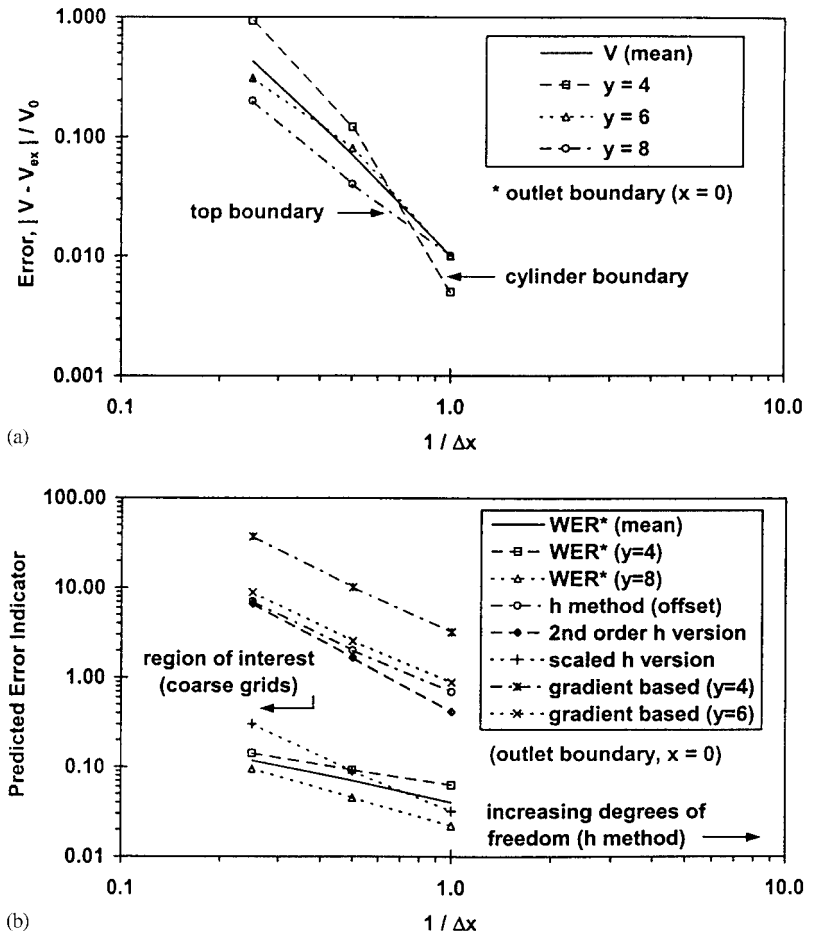

Figure 7. (a) Solution error and (b) comparison of error indicators ($x = 0$).

in the legend and the error is normalized with respect to a reference (inlet) velocity. From the numerical results, the mean velocity at the outlet approaches the expected value of 2.0 as the grid spacing decreases (i.e. $1/\Delta x$ increases). Based on an area reduction by a factor of 2 from the inlet to the outlet, it is anticipated that the mean velocity at the outlet should be twice the inlet velocity (based on conservation of mass).

Various predicted error indicators, including a non-dimensionalized WER (denoted by WER*) and other conventional error indicators, are displayed and compared in Figure 7(b) (log–log scale). The value of WER is non-dimensionalized after dividing by the fluid specific heat, c_v, and unit mass flow. In Figure 7(b), WER* is depicted at the lower edge ($y = 4$) and upper edge ($y = 8$) of the outlet boundary, as well as the mean WER* value along the exit boundary. It can be observed that WER* decreases when the grid spacing is reduced. This trend is similar to that observed with the solution errors presented in Figure 7(a). The velocity field is determined from Laplace's equation for the divergence of velocity, so the results

in Figure 7(a) represent an error in the divergence of velocity. Although the rate of WER* reduction is slower than the results in Figure 7(a), the proper trends with $1/\Delta x$ are observed. The scaling factor that sets the leftmost point of each curve is represented by the constant of proportionality inherent in the previously discussed error analysis relating the weighted truncation error and the weighted entropy residual.

Also, other types of finite-element error indicators are shown in Figure 7(b). These comparisons include methods described by Shih [16] and Babuska *et al.* [11]. Better solution accuracy is generally achieved by increasing the number of degrees of freedom, N. In the *h method*, N is raised when the mesh is refined into smaller elements, while the *p method* increases the polynomial degree of elements without subdividing the elements. When the error indicator, $\|e\|$, is defined with respect to some norm, *a posteriori* error indicators based on the h method are used as follows:

$$\|e\| = C_1 h(h^{n-1} + C_2) \tag{44}$$

where n and h refer to the order of accuracy and characteristic grid spacing, respectively. Also, C_1 and C_2 arc constants (often unknown). In Figure 7(b), an h method with an estimated offset based on values at the midpoint of the outflow boundary is depicted. Based on Equation (44) with $n = 2$, the method includes the error bounds of the interpolated function through coefficients involving the area and side length of the triangular element [16]. Further details describing *a posteriori* error estimates are given by Babuska and Rheinboldt [22], as well as Carey and Humphrey [23] regarding error bounds of variable meshes. The error indicator, as well as its second-order approximation (without the offset of the previous case), show a faster rate of decline than WER*, but at the expense of coarse grid predictions.

When values of C_1 are scaled down by a factor of 0.01, the resulting slope and magnitude are closely representative of Figure 7(a). However, the appropriate value of C_1 in this approach is generally unknown, whereas the non-dimensionalized WER* provides a physically-based method involving the magnitude for coarse grids. This feature is further clarified when the value of C_1 can be estimated from second-order derivatives of the scalar [16] at various positions of the outflow boundary, $y = 4$ and 6. This error indicator is based on the analysis of interpolation errors [15]. In those cases, the error estimates are over-predicted, particularly for coarse grids. Error indicators for coarse grids can be very important, since complex flow simulations are often too time consuming or expensive when performed on 'sufficiently refined' grids. In many cases, other error indicators are generally only accurate in the limit as the element size approaches zero and the mesh possesses certain features [24]. Thus, in many cases for a fixed grid size that is not optimally constructed and refined, conventional methods are limited and the current entropy-based approach appears to provide a viable alternative for error estimation.

It is worthwhile to closely compare the current WER*-based approach and the other error indicators. Due to its physical basis in the second law of thermodynamics, it is anticipated that a WER* type method can potentially encompass more types of numerical errors, including both overall and individual parts of the overall formulation, rather than only certain types of errors (i.e. dispersive, false diffusion [18]). Also, the second law is a widely applicable physical law, in contrast to mathematical error indicators limited to restricted classes of problems. Its generality is expected to be relevant to both *h methods* and *p methods*. While the aforementioned error indicators are generally applicable either locally or globally, the WER* predictions have a physical basis under both cases. Furthermore, various specific

Table I. (a) Comparison of WER results at outflow boundary and (b) summary of WER results.

(a)

Mesh 1		Mesh 2		Mesh 3		Normalized WER slope
Node	WER	Node	WER	Node	WER	
4	38.51	5	11.21	9	5.50	−0.31
8	80.84	35	61.51	115	36.31	−0.28
13	139.19	33	93.04	111	53.20	−0.31

(b)

	Mesh 1	Mesh 2	Mesh 3
Maximum (+) WER	139.14	93.04	53.20
Maximum (−) WER	−85.66	−36.45	−11.26
Average WER	41.23	19.26	8.10

limitations are inherent in the other error indicators: (i) often difficult or impractical to evaluate higher-order derivatives when finding C_1 and other constants, (ii) these derivatives may be unbounded and (iii) no systematic way of evaluating the constants, such as C_1, for a wide class of problems. In view of these limitations, the current entropy-based approach offers an alternative physical basis from which numerical errors can be understood and predicted.

These benefits of entropy-based error analysis can be inferred from the results in Figure 7(b). The main trends of lower WER^* values are observed when the grid is refined. It is anticipated that a slow or no rate of WER^* decline may indicate that a fundamental aspect of the numerical formulation has been incorrectly implemented. Furthermore, individual components of the overall formulation could be isolated in view of their entropy characteristics, thereby identifying local error indicators. Although this article considers inviscid flows, the concepts could be extended to viscous flows with heat transfer. In those cases, the magnitude of negative entropy production could be used as the measure of error detection, rather than absolute WER^* values in the current fluid flow example.

Furthermore, a comparison between WER (dimensional) values at equivalent nodal points in all grids (i.e. grids 1–3), as well as the variation in maximum and minimum values (with WER sign), is summarized in Table I. For example, consider all nodes along the outflow boundary in mesh 1 (i.e. nodes 4, 8, 13) and let us compare results at the same locations from results based on simulations from meshes 2 and 3. Nodes 5 (mesh 2) and 9 (mesh 3) coincide with the position of node 4 in mesh 1. Similar agreement is given for nodes 35 and 33 (mesh 2), as well as nodes 33 and 111 (mesh 3) with respect to nodes in mesh 1.

The same trend of reduced WER with grid refinement is observed in Table I(a). The slopes between values in meshes 1–2 and meshes 2–3 are normalized by dividing all values by WER values obtained in mesh 1. Then the average slope of reduced WER values for each mesh was computed. The resulting values in Table I(a) indicate than an average slope of approximately −0.3 is obtained for the rate of WER reduction. Other similarly compared slopes also generally lied within a narrow range thereby indicating that there is some direct relationship between WER reduction and solution error reduction. The significance of establishing this relationship is that numerical error is often difficult to assess whereas WER computations can be readily

added to conventional CFD codes as a complementary (or possibly corrective) part of the overall formulation.

In addition, the signs of WER (i.e. positive/negative) and average WER values (accounting for these signs) are retained and summarized in Table I(b). It can be observed that both deviations from the expected zero WER value (i.e. negative and positive deviations), as well as the average WER, are reduced when the grid spacing is refined. This result is consistent with earlier observations. Although both positive and negative deviations indicate anomalies in the case of potential flow, it is anticipated that the sign may be significant with respect to various characteristics of the solution error, i.e. diffusive error, dispersive error, second-order effects, etc. Furthermore, the sign would have a specially significant meaning for viscous flows since it would more clearly distinguish non-physical results (indicated by negative sign) from certain types of errors, such as diffusive type errors.

6. CONCLUSIONS

A Galerkin weighted residual method is presented in a finite-element analysis of computational fluid flow. A discrete formulation of the second law of thermodynamics is provided as a complementary component of the overall formulation. The entropy-based approach computes a WER and establishes its close connection to the truncation error in the solution of the mass and momentum equations. In this way, local anomalies involving mass and momentum exchange, such as velocity undershoots, can be detected by trends in the WER data. The specific slopes involving WER reduction, grid spacing and solution error have been determined to fall within a narrow range. The overall trends confirmed that truncation errors are closely related to reduced weighted entropy residual in an example of incompressible fluid flow in a converging channel. It is anticipated that entropy can serve as an effective basis for achieving reliable, accurate and physically reasonable results in computational fluid flow.

NOMENCLATURE

A	area of element
$\mathbf{F}$	entropy flux
N	interpolation (shape) function
p	pressure
$\dot{P}_s$	entropy production rate
$\mathbf{q}$	conserved variable(s)
R	residual
s	specific entropy
u, v	velocity components
V	velocity magnitude ($\sqrt{u^2 + v^2}$)
W	weight function
WER	weighted entropy residual

Greek

ϕ velocity potential
Φ nodal value of ϕ
ρ fluid density

Subscripts

G evaluation on boundary
i node i
0 reference value
s entropy

Superscripts

e local (elemental) value
$n-1$ previous time step
n current time level

ACKNOWLEDGEMENTS

The support of the Natural Sciences and Engineering Research Council of Canada in the form of a research grant to G. F. Naterer is gratefully acknowledged.

REFERENCES

1. Anderson DA, Tannehill JC, Pletcher RH. *Computational Fluid Mechanics and Heat Transfer*. Hemisphere Publishing Corp.: Washington, DC, 1984.
2. Lax PD. Hyperbolic systems of conservation laws II. *Communications in Pure and Applied Mathematics* 1957; **10**:537–566.
3. Hughes TJR, Franca L, Mallet M. A new finite element formulation for computational fluid dynamics: symmetric forms of the compressible Euler and Navier–Stokes equations and the second law of thermodynamics. *Computer Methods in Applied Mechanics and Engineering* 1986; **54**:223–234.
4. Camberos JA. A probabilistic approach to the computational simulation of gas dynamic process. *Ph.D. Dissertation*, Stanford University, 1995.
5. Naterer GF, Schneider GF. Use of the second law for artificial dissipation in compressible flow discrete analysis. *AIAA Journal of Thermophysics and Heat Transfer* 1994; **8**(3):500–506.
6. Merriam MI. Smoothing and the second law. *Computer Methods in Applied Mechanics and Engineering* 1987; **64**:177–193.
7. Naterer GF, Camberos JA. Second law formulation for a stable velocity—temperature coupling in computational fluid flow. *AIAA Paper* 99-3514, *AIAA* 30*th Fluid Dynamics Conference*, Norfolk, VA, 1999.
8. Huebner KH, Thornton EA, Byrom TG. *The Finite Element Method for Engineers* (3rd edn). Wiley: New York, 1995.
9. Akin JE. *Finite Element Analysis for Undergraduates*. Academic Press: London, 1986.
10. Becker EB, Carey GF, Oden JT. *Finite Elements*: *An Introduction*. Prentice-Hall: Englewood Cliffs, NJ, 1981.
11. Babuska I, Zienkiewicz OC, Gago J, Oliveira ER de A (eds). *Accuracy Estimates and Adaptive Refinements in Finite Element Computations*. Wiley: New York, 1986.
12. Kelly DW, Gago R, Zienkiewicz OC, Babuska J. *A posteriori* error analysis and adaptive processes in the finite element method. Part I: Error analysis. *International Journal for Numerical Methods in Engineering* 1983; **19**:1593–1619.
13. Bank RE, Sherman AH. An adaptive, multi-level method for elliptic boundary value problems. *Computing* 1981; **26**:91–105.
14. Bank RE. Multi-level iterative method for nonlinear elliptic equations. In *Elliptic Problem Solvers*, Schultz, M (ed.). Academic Press: New York, 1981.

15. Diaz AR, Kikuchi N, Taylor JE. A method for a grid optimization for finite element methods. *Computer Methods in Applied Mechanics and Engineering* 1983; **41**:29–45.
16. Shih TM. *Numerical Heat Transfer*. Hemisphere Publishing Corp.: Washington, DC, 1984.
17. Oden JT, Demkowicz L, Strouboulis T, Devloo P. Adaptive methods for problems in solid and fluid mechanics. In *Accuracy Estimates and Adaptive Refinements in Finite Element Computations*, Babuska I, Zienkiewicz OC, Gago J, Oliveira ER ed A (eds). Wiley: New York, 1986; 249–180.
18. Patankar SV. *Numerical Heat Transfer and Fluid Flow*. Hemisphere Publishing Corp.: Washington, DC, 1980.
19. Naterer GF. Constructing an entropy-stable upwind scheme for compressible fluid flow computations. *AIAA Journal* 1999; **37**:303–312.
20. Naterer GF. Predictive entropy based correction of phase change computations with fluid flow—Part 2: Application problems. *Numerical Heat Transfer B* 2000; **37**:415–436.
21. White F. *Fluid Mechanics* (2nd ed). McGraw Hill, Inc.: New York, 1986.
22. Babuska I, Rheinboldt WC. A posteriori error estimates for the finite element method. *International Journal for Numerical Methods in Engineering* 1978; **12**:1597–1615.
23. Carey GF, Humphrey DL. Mesh refinement and iterative solution methods for finite element computations. *International Journal for Numerical Methods in Engineering* 1981; **17**:1717–1734.
24. Kelly DW. The self-equilibration of residuals and upper bound error estimates for the finite element method. In *Accuracy Estimates and Adaptive Refinements in Finite Element Computations*, Babuska I, Zienkiewicz OC, Gago J, Oliveira ER ed A (eds). Wiley: New York 1986; 129–146.

